JACS JOURNAL OF THE AMERICAN CHEMICAL SOCIETY

ARTICLE

pubs.acs.org/JACS

Formation of Interpenetrating Hierarchical Titania Structures by Confined Synthesis in Inverse Opal

Benjamin Mandlmeier,[†] Johann M. Szeifert,[†] Dina Fattakhova-Rohlfing,[†] Heinz Amenitsch,[‡] and Thomas Bein*[,†]

[†]Department of Chemistry and Center for NanoScience (CeNS), University of Munich (LMU), Butenandtstrasse 11, Gerhard-Ertl-Building (E), 81377 Munich, Germany

[‡]Institute of Biophysics and Nanosystems Research, Austrian Academy of Sciences, Schmiedlstrasse 6, 8042 Graz, Austria

S Supporting Information

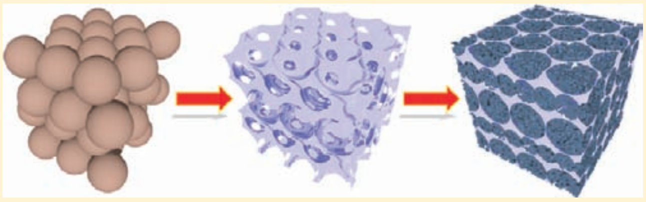

ABSTRACT: Hierarchical periodic titania nanostructures composed of a macroporous crystalline scaffold and mesoporous titania were prepared by confined synthesis. The strategy for the generation of these hierarchical structures involves preparation of inverse opal titania layers and subsequent filling of the interstitial macroporous voids with surfactant-containing titania precursors to obtain a mesostructured titania phase using the surfactant Pluronic P123. The formation of mesostructure in the confined space of the macroporous scaffold upon thermal treatment was investigated with in situ grazing incidence small-angle X-ray scattering (GISAXS). The macroporous scaffold strongly influences the mesostructure assembly and leads to much larger structural parameters of the formed mesostructure, this effect becoming more pronounced with decreasing pore size of the macroporous host. Furthermore, the inverse opal scaffold acts as a stabilizing matrix, limiting the shrinkage of the mesopores upon heating. This effect is coupled with an enhanced crystallization of the mesophase, which is attributed to the crystalline walls of the macroporous host. Sorption measurements of the final hierarchical titania structure of 5 μm thickness show that the porous system is fully accessible, has a high total surface area of 154 m^2/g, and has an average mesopore size of 6.1 nm, which is about 20% larger than the pore size of 5.1 nm for the reference mesoporous film obtained on a flat substrate. These hierarchical structures were implemented as anodes in dye-sensitized solar cells (DSCs), showing a conversion efficiency of 4% under one sun illumination, whereas the calcined macroporous scaffold alone shows an efficiency of only 0.4%.

INTRODUCTION

Metal oxides with periodic porous architecture have shown great potential in processes involving interface- and transport-related phenomena, such as adsorption, catalysis, energy conversion,[1−3] and storage,[4−6] or in biomaterials.[7−9] Tuning the chemical functionality and the morphology of the pore network provides a flexible means to optimize the performance of such materials. However, for specific applications such as those based on transport phenomena, it would be highly desirable to implement a hierarchical organization of different scales of porous frameworks in one material.

The majority of reports on the fabrication of hierarchical porous metal oxides deal with systems containing different scales of pores. Such materials, which combine large pores with walls that consist of the small ones,[7,10−12] are of interest for applications involving molecular adsorption and diffusion phenomena, and whose functionality is therefore largely governed by the properties of the pores.[7,11]

Another type of hierarchical systems involves different length scales of two different physical properties, for example, pore diameter and crystal size of a larger backbone. Such hierarchical morphologies have been much less investigated, but they are of significant interest for various applications, for example, those involving charge transfer and charge transport properties, in which the performance is determined by the electronic properties and the size of the inorganic backbone in addition to the dimensions of the porous network. Examples for these applications are new forms of hybrid or dye-sensitized solar cells, where the charge carrier diffusion length is one of the important performance-limiting factors[13−15] and whose efficiency strongly depends on the morphology of the titania layer acting as an n-conductor.[1,16,17] These devices are expected to benefit from hierarchical structures, because the latter provide the combination of both larger structural elements for high carrier conductivity over greater length scales and very small ones for achieving large interface areas. Moreover, an additional possible increase in the light harvesting efficiency can be achieved due to photonic or backscattering effects resulting from periodic macroscopic structures.[18−21] However, these effects were not a focus of the present study. Nanotube arrays, rods, and inverse opals are examples for such large macroscopic titania morphologies that

Received: May 21, 2011
Published: September 02, 2011

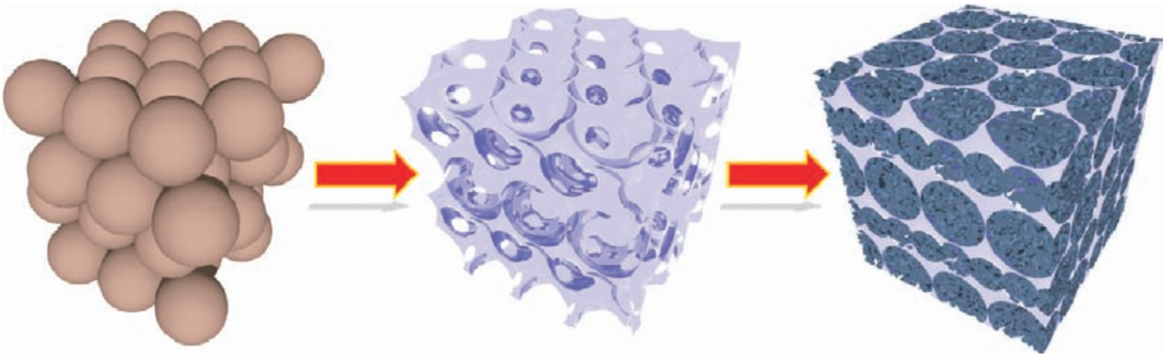

Figure 1. A strategy for the preparation of hierarchical titania frameworks: a colloidal crystal template is impregnated with a titania precursor solution and forms a three-dimensional ordered macroporous material (3 DOM) after template removal. The inverse opal host is filled with the surfactant-containing solution of hydrolyzed titania, leading to the formation of a hierarchical titania framework after calcination.

demonstrate excellent electron transport properties due to optimized orientation with respect to the current collector, or large crystal size with few grain boundaries.[6,22−28] On their own, however, these structures feature interface areas that are too low for efficient electrodes in photovoltaic applications. On the other hand, sensitized mesoporous crystalline titania films show impressively high light absorption in thin layers[29−33] but limited electron transport characteristics due to the small size of the crystals (and grain boundaries) composing the mesoporous scaffold.[34]

Therefore, a hierarchical architecture combining advantages of both mesoscale and macroscale morphologies, that is, efficient light harvesting and charge separation in mesoporous phases and fast transport of photogenerated electrons through interpenetrating macroscale scaffolds, is expected to offer (i) new insights into the impact of morphology on charge carrier dynamics, and (ii) new opportunities for the design of efficient DSCs.

Reports concerning the fabrication of crystalline hierarchical titania are scarce and are mostly based on the control of growth conditions leading to the simultaneous formation of hierarchical titania frameworks.[2,22,35,36] An alternative approach is a combination of individual strategies for the fabrication of large-scale and mesoscopic materials. This general method would offer the possibility to individually vary both the macro- and the mesostructures' morphologies and dimensions, as was demonstrated for hybrid hierarchical oxides obtained by infiltration of mesoporous amorphous silica in macroporous ceramic[37] or titania backbones.[38] This strategy has not yet been applied to the fabrication of fully crystalline hierarchical titania. In this context, the following questions will be important: How does one ascertain that the desired mesoporous structures can be formed in a confined space? How does one ensure the crystallization of a mesophase, when the regular mesostructure without a confining backbone collapses upon heating to the critical temperature for crystallization? What is the connectivity of porous systems and the accessibility of pore volume deep within the layers?

Here, we report the fabrication of hierarchical structures based on the preparation of a highly crystalline, macroporous inverse opal backbone that is formed by colloidal crystal templating using polymethylmethacrylate (PMMA) spheres, and a titania precursor solution for impregnation. These macropores are afterward filled with a mesoporous titania phase by impregnation with a titania precursor solution containing a polymer template (Figure 1). The development of the mesostructure from this surfactant-directed evaporation-induced self-assembly method was monitored by in situ GISAXS measurements and correlated with electron microscopy data. An interesting confinement effect of the macroporous backbone on the mesostructure leads to enhanced temperature stability, less shrinkage, and generally large mesopore sizes, as was observed for the two investigated pore sizes of the macroporous scaffold. Furthermore, we found that the highly crystalline backbone of the macroporous titania scaffold synergistically affected the crystallization behavior of the sol−gel derived mesoporous filling. The resulting hierarchical structures were also investigated as anodes in dye-sensitized solar cells, demonstrating the large difference between the individual components and the combined hierarchical titania structure with respect to photon to electron conversion efficiency.

RESULTS AND DISCUSSION

For the preparation of the macroporous host scaffold, opal films of PMMA spheres were initially assembled on different substrates by a horizontal deposition from aqueous colloidal dispersions (Figure 1).

The size of the PMMA spheres can be controllably varied from around 100 to 400 nm by selection of surfactant concentration and reaction time in emulsion polymerization synthesis,[39] and the thickness of the opal layers by the concentration of the PMMA spheres and the amount of the applied dispersion. The dried films obtained in this way show an ordered close packing of the larger PMMA spheres and a more loose packing for the smaller ones, as can be seen from the SEM images (Figure S1a,b in the Supporting Information). In a second step, the negative replica of the opal material was fabricated by infiltration of the films with a solution of titania sol using a dip-coating technique according to a known procedure.[40] As can be seen from the EDX mapping of the films' cross sections (Figure S1), a single impregnation step already leads to a complete filling of the interstitial voids between the PMMA spheres. The good filling quality can be attributed to a good wetting behavior of the sulfonated PMMA spheres, causing the transport of the titania precursor into the voids by capillary forces. After the infiltrated films were dried, the PMMA spheres were removed by calcination in air at 400 °C, which also leads to the crystallization of the titania scaffold. The inverse opals obtained in this way are assigned further as Macro-*X*, with *X* standing for the diameter of the parent PMMA spheres in nanometers (see Table 3 in the Experimental Section).

SEM and TEM images of the films obtained in this way using the 200 ± 25 nm PMMA spheres reveal the presence of 3 DOM

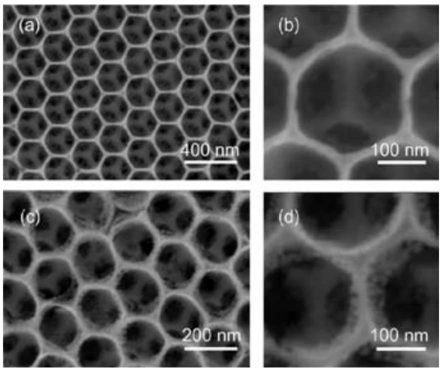

Figure 2. FESEM micrographs (top view) show the morphology of the macroporous titania inverse opal prepared by the 200 nm large PMMA spheres before (a, b, sample Macro-200) and after a single dip coating step with a Pluronic P123-containing titania sol−gel solution, leading to the formation of a thin mesoporous titania layer on the crystalline inverse opal backbone (c, d, sample Hier-200-dc). All films were prepared on silicon substrates and calcined at 400 °C.

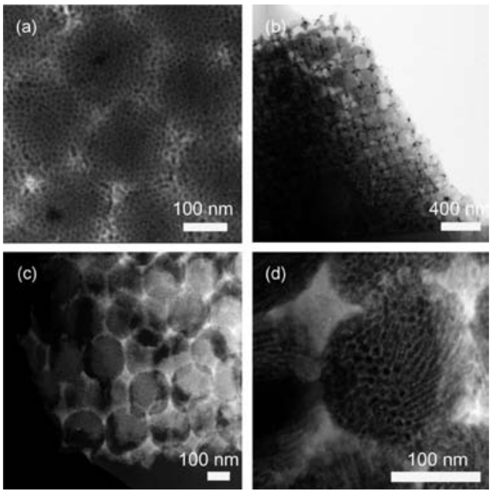

Figure 3. Electron micrographs of hierarchical titania frameworks fabricated using 200 nm PMMA spheres (Hier-200-ca): FESEM top-view image (a), and micrographs of the films' cross sections in TEM (b) and HAADF-STEM (c,d). The brighter areas in (a), (c), (d) and the darker spots in (b) correspond to larger titania crystals in the dense walls of the inverse opal. All films were prepared on silicon substrates and calcined at 450 °C.

macroporous structure of a highly ordered crystalline titania scaffold containing interconnected spherical voids with a diameter of around 200 nm and intervoid connections of around 50−70 nm (Macro-200, Figure 2a,b and Figure S2).

For the fabrication of the hierarchical structure, the macroporous titania films were filled with a surfactant-containing solution of hydrolyzed titania precursors using different techniques. Casting of this solution by dip coating results in an open hierarchical structure containing the macroporous scaffold homogeneously covered by an additional layer of mesoporous titania (assigned as Hier-200-dc, Figure 2c,d). To achieve complete filling of the macropores, the solution for the mesoporous phase was drop-cast into the inverse opal host layer. The amount of the solution was calculated from the available macropore volume in the inverse opal scaffold as estimated from the pore diameter and the films' thickness (see detailed description in the Experimental Section). The filled films were dried in air and calcined at temperatures of 200−450 °C applying a fast calcination ramp (10 °C min^{-1}). SEM top view and TEM cross-section images show that this procedure leads to filling of each macropore throughout the whole film thickness, resulting in the formation of mesoporous films periodically interpenetrated with the macroporous scaffold, such that both mesoscale and macroscale repeating units are observed in the electron microscopy images (assigned as Hier-200-ca, Figure 3a,b). The thickness of the films is determined by the thickness of the parent macroporous scaffold (about 5.5 μm). We note that coating of the solutions for the mesoporous film preparation alone enables fabrication of no more than 1 μm thick films on a flat substrate; attempts to increase the film thickness further result in the films' cracking and peeling off the substrates.[33,41] The fact that the thickness of mesoporous films can reach several micrometers in a hierarchical structure is attributed to good adhesion between the crystalline titania mesophase and the dense polycrystalline three-dimensional macroporous titania. The hierarchical titania films are completely crystalline after calcination in air at 450 °C and consist of anatase, as derived from their wide-angle X-ray scattering (WAXS) patterns, high-resolution TEM (HR-TEM) images, and selected area electron diffraction (SAED) patterns of the films' cross sections (Figure 4). The HR-TEM images reveal that the obtained hierarchical structure is composed of two types of crystalline anatase, with crystal sizes of over 20 nm in the macroporous titania walls (Figure 4a) and 4−6 nm in the walls of mesoporous material. The corresponding SAED pattern (Figure 4d) proves the existence of these two size populations of the anatase crystals in the hierarchical sample. In addition to the broad diffraction rings originating from many

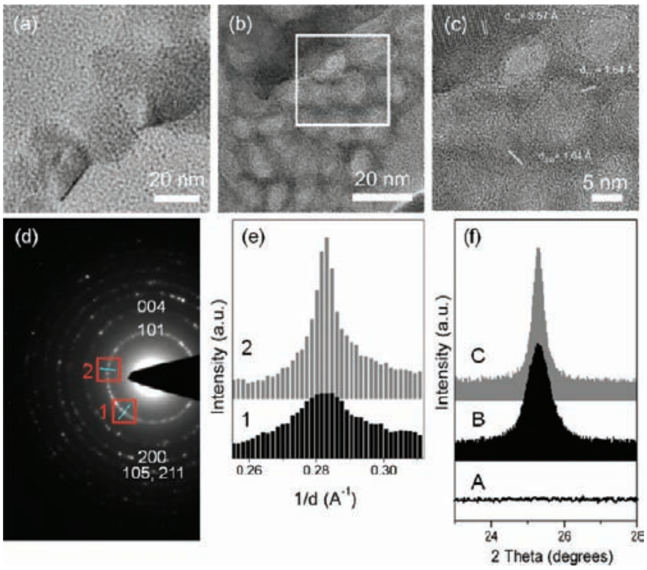

Figure 4. Structural characterization of titania films. TEM micrographs of the crystalline macroporous (a, Macro-200) and hierarchical titania films (b, c, Hier-200-ca) after calcination at 400 °C (a) and 450 °C (b,c). The diffraction rings in the SAED pattern (d, Hier-200-ca) could be indexed with the anatase phase. The corresponding intensity profiles of the anatase (101) reflection at two different positions (d1, d2) show the presence of two sizes of crystalline domains (e). WAXS patterns (f) of the hierarchical film (B) and individual mesoporous (A, Meso) and macroporous (C, Macro) materials prepared under the same conditions.

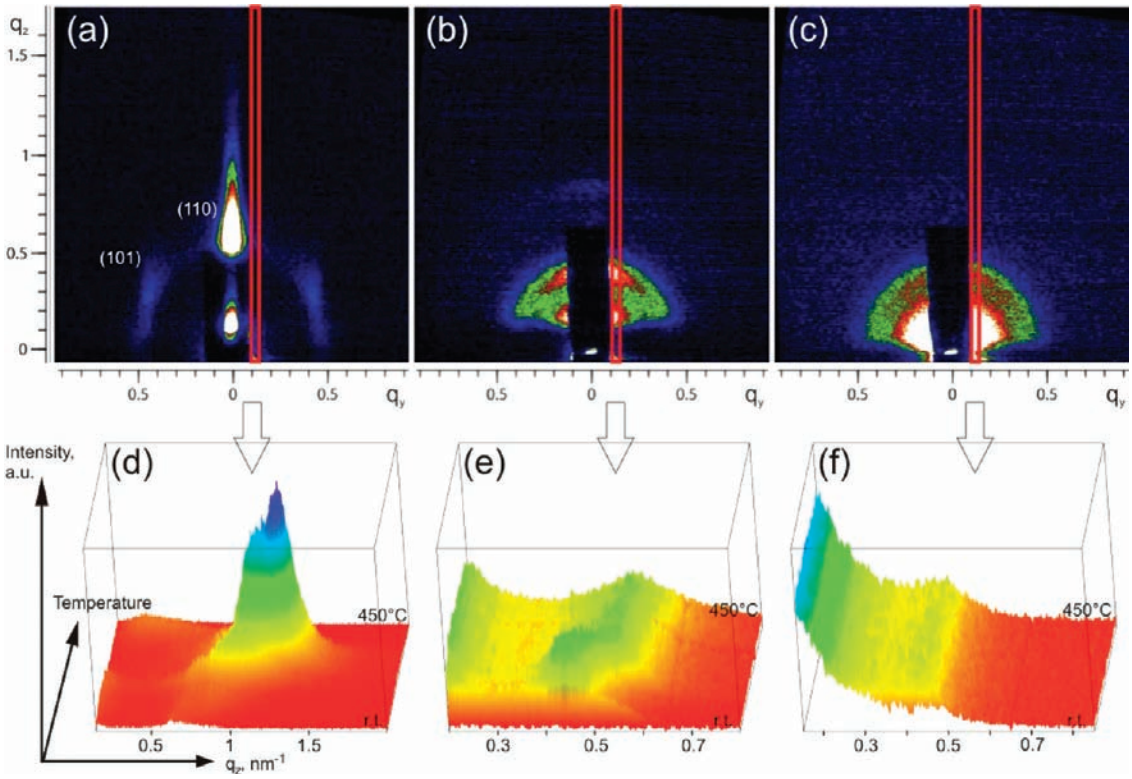

Figure 5. In situ investigation of the evolution of hierarchical titania (Hier-200-ca, Hier-100-ca). 2D-GISAXS patterns of samples made by casting a solution of Pluronic P123-containing titania sol on flat silicon (a), into macroporous titania with 200 nm (b, Macro-200) and 100 nm (c, Macro-100) pore size after drying at room temperature (note that the reflections of the periodic structures of the inverse opal are not visible because of their close proximity to the primary beam). Second row: Development of the diffraction peaks in the 2D-GISAXS patterns made visible by comparing 1D-intensity profiles at a constant q_y-value of 0.12−0.15 nm^{-1} (highlighted in red in 2D-images) during in situ heating to 450 °C: film from solution with Pluronic P123-containing titania sol cast on flat silicon (d, Meso). Same solution cast into an inverse opal with 200 nm (Macro-200, e) and 100 nm (Macro-100, f) pore size. Electron microscopy shows that the mesoporous titania completely penetrates into the macroporous scaffold and that it does not form a superficial layer (see also Figure 3).

randomly oriented small crystals within the mesostructure (intensity profile over (101) anatase diffraction, number 1 in Figure 4e), the large crystals in the walls of the macroporous host scaffold lead to bright spots of the same phase but with a much smaller width superimposed on the broad ring (intensity profile number 2). In WAXS, the unfilled macroporous host layer exhibits a peak broadening of the (101) anatase diffraction corresponding to a mean crystal size of about 30 nm. After filling with the mesoporous titania phase, the line broadening of the hierarchical structure becomes much larger, and the mean crystal size from the full width at half-maximum can now be calculated as 18 nm.

This apparent reduction of crystal size can be explained by the coexistence of two populations of crystal sizes in the hierarchical structure: large ones (over 30 nm) in the walls of the macroporous backbone and small ones (smaller than 10 nm) in the mesoporous filling. Strikingly, the pure mesoporous titania (assigned further as Meso) phase prepared as a reference on a flat substrate remains amorphous as a result of the applied heating conditions (Figure 4f, A, and TEM images, Figure S3). We conclude that the highly crystalline backbone has a strong synergistic effect on the crystallization of the mesoporous filling, acting as a nucleation site for further crystallization of the initially amorphous titania phase. We have previously observed similar effects for titania nanoparticles dispersed in a sol−gel matrix; thus it appears that this behavior can be generalized.[30]

To further investigate the effect of this hierarchy, and especially the influence of the confined space in the macroporous material on the evaporation-induced self-assembly (EISA)-based formation of a templated titania sol−gel mesostructure, we performed 2D-GISAXS monitoring of mesostructure evolution using in situ heating experiments (Figure 5 and Figure S4). A small amount of the solution for the mesoporous phase was drop-cast on a substrate, dried, and subsequently heated to 450 °C. As substrates, we examined two different macroporous titania films with pore sizes of about 100 nm (Macro-100) and 200 nm (Macro-200), respectively. A flat Si wafer was used as a reference (Meso).

The 2D-GISAXS patterns of the mesoporous structure on flat silicon (Figure 5a,d) show a well-ordered cubic structure with reflections in the q_z- and q_y-plane. The corresponding *d*-spacings at room temperature are 9.5 nm (in-plane, q_z) and 10.4 nm (out-of-plane, q_y). In the confined space of a macroporous inverse opal of 200 nm pore size (Hier-200-ca, Figure 5b,e), the pattern of the mesostructure exhibits a slightly broadened peak of a preferred in-plane (q_z) orientation only, with a significantly larger *d*-spacing of 12.7 nm. The mesostructure in the smaller pore inverse opal Hier-100-ca (Figure 5c,f) is much less ordered, and only an indication of a reflection in the q_z plane can be seen. The shape of the pattern and the mesostructure's dimension are similar to those of the 200 nm inverse opal sample (Figure 4).

Upon heating the films, they show drastically different shrinkage behavior. This can be seen from the shifts of the diffraction

Table 1. **Comparison of the *d*-Spacing of the Mesoporous Structures on a Flat Si Substrate and in Macroporous Inverse Opals with 200 and 100 nm Pore Size before and after Heating to 450 °C**

		flat substrate (Meso)		200 nm macropores (Hier-200-ca)	100 nm macropores (Hier-100-ca)
	temperature	in-plane	out-of-plane	in-plane	in-plane
d-spacing [nm]	20 °C	9.5	10.4	12.7	12.7
	450 °C	5.8	7.4	10.1	11.1
shrinkage		39%	29%	21%	12.6%

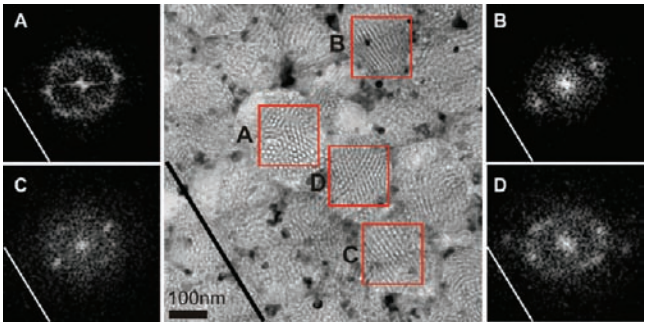

Figure 6. TEM image of the hierarchical titania film (Hier-200-ca) prepared in macroporous titania with 200 nm pore size (Macro-200), and FFT images (A−D) of selected areas showing the periodic organization of mesopores in single macropores. The white lines show the position of substrate with respect to the film.

peaks (3D graphs illustrating the thermal development of intensity profiles at a fixed value of q_y, Figure 5d−f). Heating the mesoporous film on flat silicon results in a drastic shrinkage of the porous structure by 39% of the in-plane and 29% of the out-of plane reflection, respectively (see Figure 5 and Table 1). The mesostructures filled into the inverse opals show much less shrinkage upon heating, resulting in a structural contraction of only 21% (Hier-200-ca) and 13% (Hier-100-ca), respectively.

Judging from these data, the macroporous framework obviously influences the assembly of the mesostructure and leads to much larger structures (22% increase at room temperature) with a different orientation. A similar phenomenon has been described for the mesostructure formation in large pore anodized alumina materials, but the universality of this effect has not yet been shown concerning other macrostructures such as inverse opals.[42−45] Furthermore, the inverse opal backbone acts as a stabilizing matrix, limiting the shrinkage of the mesopores upon heating. In this way, the final size of the mesopores in the smallest macroporous matrix is even 50% larger than that of a structure made from the same solution on a flat substrate.

The films monitored by GISAXS were further investigated by electron microscopy. The TEM images of the cross sections of the hierarchical titania films reveal that a mesoporous phase is formed in each pore of the macroporous host (Figure 6). The mesoporous material shows a high order of periodicity within individual macropores, such that the mesoporous phase formed within most of the macropores can be considered as a single mesostructural domain (see orientational peaks in the Fourier transforms (A−D) of highlighted sections in Figure 6). Between neighboring macropores, there seems to be little orientational relationship of the mesostructure, but the observed orientations reflect some dependence with respect to the substrate. The periodic structures, their Fourier transforms, and the corresponding *d*-spacings are in good agreement with the results of the GISAXS measurements. The TEM images of the reference mesoporous titania film obtained under the same conditions on a flat Si substrate in the absence of macroporous host (Figure S3 in the Supporting Information) show the formation of the periodic cubic mesostructure with significantly smaller *d*-spacing, confirming the GISAXS observations.

The porosity of the different titania materials was additionally characterized by nitrogen sorption measurements. The parent macroporous titania (Macro-200) films exhibit, as expected, type II isotherms typical for the macroporous material and a low surface area of 64 m^2/g (Figure 7a, A). The character of porosity, however, changes completely after the filling of the macroscopic pores with the mesoporous titania. The isotherms of the resulting hierarchical films (Hier-200-ca) feature a step at relative pressures around 0.6−0.7 p/p_0 corresponding to the filling of the pores in the mesoporous range, a largely increased surface area of 154 m^2/g, and a narrow hysteresis between adsorption and desorption branches, indicating the uniform pore size distribution (Figure 7a, B). At first glance, the adsorption behavior of the hierarchical material is very similar to that of the mesoporous titania film obtained on a flat substrate without the macroporous scaffold (Figure 7a, C). However, close inspection of the two latter materials reveals differences in their adsorption characteristics. The pore size calculated by a DFT method corresponds to 5.1 nm for a mesoporous film grown on a flat substrate. The pore size increases to about 6.1 nm when the same solution is cast into the macroporous support. The increase in the pore size in the hierarchical material is accompanied by an increase in the pore volume (from 0.24 to 0.28 cm^3/g) and a decrease in the surface area (from 210 to 154 m^2/g) as compared to the reference mesoporous film. The increase in the pore size by 16−20% for a mesoporous phase formed inside the macroporous host is in good agreement with the observations of the GISAXS and TEM methods described above. The obtained isotherms reveal the open and accessible character of porosity obtained after filling of the macropores with the solution for the mesoporous phase and also confirm that the confined space of the macroporous host has a pronounced effect on the formation of the mesoporous phase.

The above hierarchical titania layers (Hier-200-ca) were also employed as active electrodes in dye-sensitized solar cells (Figure 8) and compared to the unfilled macroporous scaffold. The macroporous scaffold exhibits a very high open circuit potential of 910 mV, indicating efficient charge collection. In the hierarchical structure, this potential is reduced to 780 mV, which can be explained by the higher amount of recombination sites due to the high surface area of the mesoporous titania filling. However, at the same time this large surface area causes a drastic increase of photocurrent density from 0.97 to 7.17 mA cm^{-2} and a change in fill factor from 0.52 to 0.71. As a

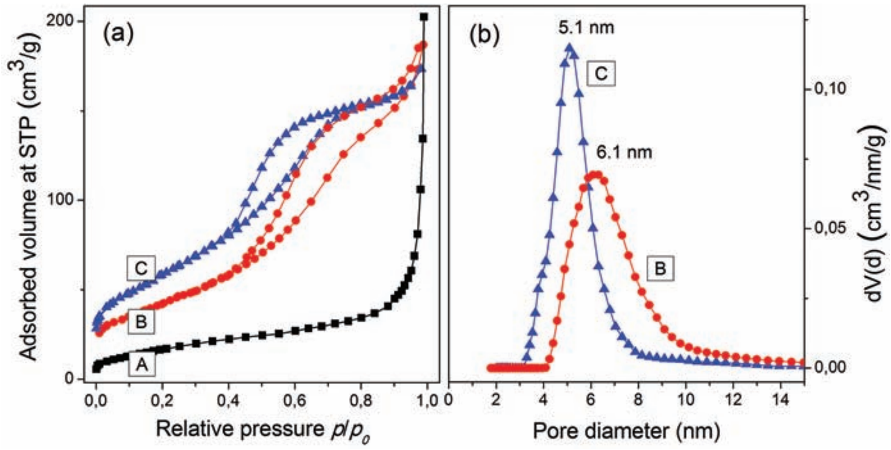

Figure 7. Nitrogen sorption isotherms (a) and DFT pore size distributions (b) of the macroporous film templated with the 200 nm latex spheres (A, Macro-200), corresponding hierarchical film after filling of the macropores with the mesoporous titania (B, Hier-200-ca), and the reference mesoporous film coated on the flat substrate (C, Meso). All of the films were calcined at 450 °C. The measurements were performed on layers removed from the substrate.

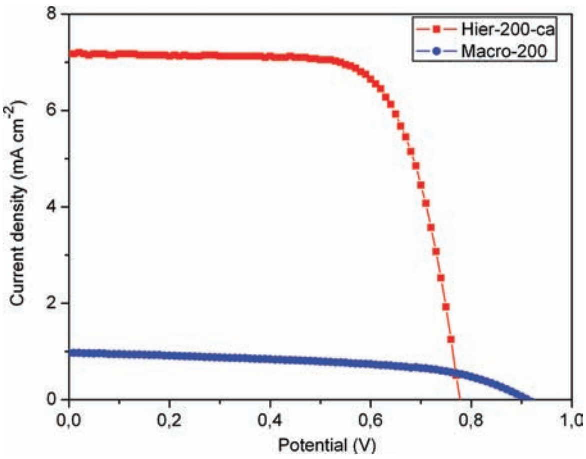

Figure 8. Photocurrent−voltage curve of DSC devices based on the inverse opal titania layers (blue, Macro-200) and hierarchical titania layers (red, Hier-200-ca), N719 sensitizer, and a volatile redox electrolyte. The titania layer thickness was about 5.5 μm. The photovoltaic performance was measured at air mass 1.5 (100 mW/cm^2) full sunlight illumination. The active cell area was 0.196 cm^2.

Table 2. Detailed Photovoltaic Parameters and EQE Values of the DSC Device Based on the Inverse Opal and Hierarchical Titania Layers 5.5 μm in Thickness, in Combination with a N719 Sensitizer and a Volatile Redox Electrolyte under AM 1.5 Sunlight at 100 mW/cm^2 Full Sun Irradiation

titania layer	J_{sc}, mA/cm^2	V_{oc}, mV	FF, %	η, %	EQE$_{530nm}$, %
Hier-200-ca	7.17	780	71.4	4.0	23.6
Macro-200	0.97	910	52.6	0.46	5.2

result, the hierarchical structure exhibits a nearly 10 times higher conversion efficiency of 4.0% as compared to the unfilled macroporous DSC with an efficiency around 0.4%.

In addition to the $I-V$ characterization, the external quantum efficiency (EQE) of the different photoanode morphologies was determined to elucidate the influence of the macroporous backbone (see Figure S5). The DSC hierarchical device (Hier-200-ca) has a higher density and surface area as compared to the unfilled macroporous device and shows an increased EQE in the characterized spectral range. At an illumination wavelength of 530 nm, Hier-200-ca has an EQE of about 24%, more than 4 times higher than the Macro-200 sample (Table 2). The normalized spectral EQE data exhibit slightly broader and shifted features and increased relative EQE values in the blue and in the red (Figure S5), which could possibly be attributed to scattering effects. We note that a significant contribution of the photonic crystal structure to the EQE data is rather unlikely with the systems under study. While the hierarchical systems show good long-range order of the macropore structure, filling the titania-based macropores with porous titania is expected to reduce the refractive index contrast such that photonic effects will be small. On this account, the most important impact of the hierarchical structure is expected to be the high surface area combined with favorable transport properties.

■ CONCLUSIONS

We have developed a strategy for the preparation of a novel type of hierarchical periodic titania nanostructures, composed of a macroporous crystalline scaffold accommodating a mesoporous titania phase. The synthetic approach for these hierarchical structures involves the preparation of inverse opal titania layers followed by the impregnation of interstitial macroporous voids with surfactant-containing titania precursors. This procedure leads to filling of all macropores through the whole film thickness, and formation of a mesoporous phase in each pore of the macroporous host. As follows from in situ GISAXS, TEM, and nitrogen adsorption measurements, the macroporous framework significantly influences the mesostructure assembly and leads to much larger structural parameters of the mesostructure. The confinement effect of the macropores on the mesostructure formation becomes more evident with decreasing pore size of the macroporous host. The inverse opal backbone acts as a stabilizing matrix, limiting the shrinkage of the mesopores upon heating, so that the final size of the mesopores in the macroporous matrix is up to 50% larger than that of a structure made from the same solution on a flat substrate. Furthermore, the

Table 3. Overview on the Used Sample Codes and the Corresponding Preparation Characteristics

sample code	structure	template	film preparation
Meso	mesoporous	Pluronic P123	casting
Macro-100	macroporous	PMMA spheres (ca. 100 nm)	CCT[a]
Macro-200	macroporous	PMMA spheres (ca. 200 nm)	CCT
Hier-100-ca	hierarchical	(1) PMMA spheres (ca. 100 nm) (2) Pluronic P123	(1) CCT (2) casting
Hier-200-ca	hierarchical	(1) PMMA spheres (ca. 200 nm) (2) Pluronic P123	(1) CCT (2) casting
Hier-200-dc	hierarchical	(1) PMMA spheres (ca. 200 nm) (2) Pluronic P123	(1) CCT (2) dip-coating

[a] CCT: Colloidal crystal templating.

highly crystalline macroporous backbone has a synergistic effect on the crystallization of the mesoporous filling, acting as a nucleation site for further crystallization of the initially amorphous titania phase. The hierarchical titania films are completely crystalline after calcination in air at 450 °C and consist of two types of crystalline anatase domains, with crystal sizes of over 20 nm in the macroporous titania walls and about 4−6 nm in the walls of mesoporous material. Sorption measurements of the final hierarchical layers of 5.5 μm thickness show that the resulting porous system is fully accessible, has a high total surface area of 154 m^2/g, and has an average mesopore size of 6.1 nm, which is about 20% larger than the pore size of 5.1 nm for the reference mesoporous film obtained on a flat substrate.

We suggest that this hierarchical architecture combining the advantages of both mesoscale and macroscale morphologies, an efficient light harvesting and charge separation in mesoporous titania, and efficient transport of photogenerated electrons through interpenetrating macroscale titania scaffold, could contribute to increasing the light conversion efficiency of dye-sensitized solar cells (DSC). Moreover, future hierarchical systems based on different materials featuring significant refractive index contrast could add additional features such as photonic crystal and backscattering effects that would contribute to the enhancement of overall light conversion efficiency.

■ EXPERIMENTAL SECTION

Materials. Methyl methacrylate (99%, MMA), sodium dodecyl sulfate (SDS), tetraethyl orthotitanate (technical grade), concentrated HCl (37% in water), Pluronic P123, and the organic solvents were obtained from Aldrich and used without further purification. Bidistilled water (Milipore Q) was used for synthesis.

An overview on the different structured titania films is summarized in Table 3.

Preparation of PMMA Spheres and Macroporous Titania Inverse Opals (Macro). Polymethylmethacrylate (PMMA) spheres sized 200 nm were synthesized by emulsion polymerization according to a procedure described elsewhere.[39] Briefly, MMA (17.8 g) and SDS (5.0 mg) were added under stirring into water (98.0 mL), which had been deoxygenated by purging with nitrogen at 40 °C for 15 min under reflux conditions. The emulsion was heated at 90 °C for 1 h; afterward, the polymerization was initiated by injection of a solution of potassium peroxydisulfate (56.0 mg) in water (2 mL), and the reaction mixture was heated at 90 °C for additional 2.5 h. The reaction was stopped by external ice cooling, and the reaction mixture was further stirred under atmospheric conditions for 30 min. The suspension of PMMA spheres was filtered and washed by repeated steps of centrifugation and ultrasonic redispersion in water. A stock solution (10 wt %) was stored at room temperature for further deposition. For the synthesis of ca. 100 nm large PMMA spheres, MMA (6.9 g) and SDS (24.5 mg) were dissolved in 98 mL of water and $K_2S_2O_8$ (56.8 mg) in 2 mL of water. MMA was polymerized and PMMA washed accordingly.

Colloidal crystal films were obtained by deposition of the PMMA spheres from aqueous solutions (1−5 wt %) on various substrates by horizontal sedimentation under vibration-free conditions. The substrates were first cleaned by ultrasonication for 30 min in a mixture of acetone and ethanol (1:1 v/v) and then in water, and dried in a stream of nitrogen.

Titania inverse opals were fabricated by dip coating (immersion time 30 s, withdrawal speed 1.3 mm s^{-1}) of the colloidal crystal films into a titania precursor solution prepared by addition of 1.08 mL (37%, 13.2 mmol) of HCl to 1.68 g (7.36 mmol) of tetraethyl orthotitanate under ice cooling and moderate stirring, followed by addition of 4.8 g (104.2 mmol) of ethanol. The impregnated films were dried at 60 °C for 1 h and then calcined in two sequential steps at 300 and 400 °C (the heating rate and dwell time for each step are 2 °C min^{-1} and 2 h, respectively).

Preparation of Mesoporous Titania Films (Meso). The solution for deposition of mesoporous titania films was prepared by a procedure described elsewhere.[46] Briefly, a solution of Pluronic P123 (0.5 g, 0.1 mmol) in ethanol (6 g) was added to a mixture of hydrochloric acid (37%, 1.05 mL, 12.8 mmol) and tetraethyl orthotitanate (1.5 mL, 7.06 mmol) at room temperature under continuous stirring for 1 h. The prepared solution was then cast on a silicon substrate (Meso-ca) or dip-coated (Meso-dc) under ambient conditions, dried at room temperature, and individually calcined up to 450 °C in air using either fast ramp (10 °C min^{-1}) or slow ramp (0.7 °C min^{-1}), dwell time 30 min.

Preparation of Hierarchical Titania Films (Hier). The templated titania precursor solution (Meso solution, see above) was cast on the inverse opal film and allowed to dry horizontally at ambient conditions at room temperature. The amount of solution used was estimated from the volume of the voids in the initial macroporous host film, taking into account the porosity and thickness of the macroporous film, and the porosity and density of the mesoporous titania phase formed after calcination. As an example, for a macroporous film of 1 cm^2 area and 1 μm thickness, the void volume can be estimated as 7.5×10^{-5} cm^3. The mesoporous phase after calcination is assumed to have 50% porosity;[31] therefore, taking into account the density of crystalline anatase of 4 g cm^{-3}, the amount of titania formed in the macropores should be 0.15 mg (1.9×10^{-3} mmol), which corresponds to 1.34×10^{-3} mL of 1.42 mol/L precursor titania solution. The films were dried at 60 °C for 1 h, and the surfactant was removed by calcination at 450 °C for 30 min (ramp: 0.7 °C min^{-1}).

For photovoltaic measurements,[47] the titania films were fabricated on FTO-coated glass substrates coated with a dense titania blocking layer. The blocking layer was prepared by spin coating (4000 rpm) of the solution obtained from hydrochloric acid (37%, 0.75 mL, 9.13 mmol), tetraethyl orthotitanate (1.05 mL, 5.06 mmol), and tetrahydrofuran (14 mL), and calcination to 450 °C (ramp: 0.7 °C min^{-1}). After preparation and final calcination of the different porous titania structures, the films were cooled to ca. 80 °C, immersed into a dye solution at room temperature, and kept there for 12 h. The dye solution contains 0.5 mM of ruthenium 535 bis-TBA dye (N 719) in acetonitrile and *tert*-butyl alcohol (volume ratio: 1:1). The dye-coated mesoporous TiO_2 films were assembled and sealed with a thin transparent hot-melt Surlyn

1702 ring with an open area of 0.196 cm^2 (DuPont) to the counter electrodes (Pt on FTO glass, chemical deposition from 0.5 mM hexachloroplatinic acid in ethanol, heated at 400 °C for 15 min). The electrolyte was injected into the inner electrode space from the counter electrode side through a predrilled hole, and then the hole was sealed with a Surlyn sheet and a thin glass cover slide by heating. The volatile electrolyte contains butylmethylimidazolium iodide (BMII, 0.536 mL, 3.0 mmol), iodine (38.1 mg, 0.3 mmol), guanidinium thiocyanate (59.1 mg, 0.5 mmol), and 4-*tert*butylpyridine (837.8 mg, 6.2 mmol) dissolved in valeronitrile (0.75 mL, 7.2 mmol) and acetonitrile (4.25, 80.7 mmol).

Characterization. Scanning electron microscopy (SEM) was performed on a JEOL JSM-6500F scanning electron microscope equipped with a field emission gun, at 4−10 kV, and an Oxford analysis system. High-resolution transmission electron microscopy (HRTEM) and scanning transmission electron microscopy in high-angle annular dark-field mode (STEM-HAADF) were performed using a FEI Titan 80-300 equipped with a field-emission gun operated at 300 kV. Cross sections of the films were prepared by epoxy glue embedding, dimple grinding, and polishing with argon ions.

The film thickness was measured by profilometry (Veeco Dektak 156) and SEM cross-section analysis.

X-ray diffraction analysis was carried out in reflection mode using a Bruker D8 diffractometer, using Ni-filtered Cu K_α radiation (wavelength: 1.5406 Å) with theta/theta geometry, operating at 40 kV and 40 mA, and a scintillation detector.

Grazing-incidence small-angle X-ray scattering (GISAXS) experiments were performed at the Austrian SAXS beamline BL 5.2 L facility at Synchrotrone Elettra (Trieste, Italy). The wavelength of the incident beam was 0.15498 nm (8 keV), and the sample−detector distance was set to 1430 mm. The detector was a two-dimensional image intensified CCD detector (model CV 12, Photonic Science Ltd., Millham, UK). The samples were heated on a modified hot stage (model DHS 900, Anton Paar).

Nitrogen sorption measurements were performed on all samples with a Quantachrome Instruments NOVA 4000e at 77 K. Pore size distribution and volume were calculated with a NLDFT equilibrium model of N_2 on silica. The specific surface area was estimated using a BET model in the range $0.02 - 0.5\ p/p_0$.

Photovoltaic measurements were done with an AM 1.5 sun simulator. A Solar Light Co. xenon lamp (model: 16S-300-V3, 100 mW/cm^2) was used as light source. $I-V$ curves were measured with a ZAHNER Electric IM6ex potentiostat and the ZAHNER Electric software Thales 4.05 USB.

External quantum efficiency measurements were performed using a 150 W xenon lamp (Lot Oriel xenon lamp) and a monochromator (Horiba Jobin Yvon microHR; slit opening fixed at 1.5 mm) with appropriate long-pass filters as the primary illumination source and a bias illumination provided by a solar simulator, which was reduced to about 10 mW/cm^2 using a neutral density filter. The primary beam was chopped at 2 Hz. The signal was detected using a Signal Recovery dual-phase lock-in amplifier (Signal Recovery, model 7265). EQE measurements were referenced to a silicon photodiode with known spectral response.

■ ASSOCIATED CONTENT

Ⓢ Supporting Information. Characterization of PMMA spheres (SEM), titania sol−gel impregnated PMMA film (EDX), macroporous and mesoporous titania (TEM), hierarchical and mesoporous titania films (2D-GISAXS), and EQE measurements of the DSC devices. This material is available free of charge via the Internet at http://pubs.acs.org.

■ AUTHOR INFORMATION

Corresponding Author
bein@lmu.de

■ ACKNOWLEDGMENT

We acknowledge funding for this project in the context of the Excellence Initiative (DFG) and the NIM Graduate Program and CeNS for supporting this work. We thank Dr. Steffen Schmidt, Tina Reuter, and Andreas Zürner for TEM, analytical measurements, and graphic design.

■ REFERENCES

(1) O'Regan, B.; Graetzel, M. *Nature* **1991**, *353*, 737.

(2) Sauvage, F.; Di Fonzo, F.; Li Bassi, A.; Casari, C. S.; Russo, V.; Divitini, G.; Ducati, C.; Bottani, C. E.; Comte, P.; Graetzel, M. *Nano Lett.* **2010**, *10*, 2562.

(3) Qu, Y.; Zhou, W.; Pan, K.; Tian, C.; Ren, Z.; Dong, Y.; Fu, H. *Phys. Chem. Chem. Phys.* **2010**, *12*, 9205.

(4) Xu, J.; Wang, K.; Zu, S.-Z.; Han, B.-H.; Wei, Z. *ACS Nano* **2010**, *4*, 5019.

(5) Chen, J. S.; Tan, Y. L.; Li, C. M.; Cheah, Y. L.; Luan, D.; Madhavi, S.; Boey, F. Y. C.; Archer, L. A.; Lou, X. W. *J. Am. Chem. Soc.* **2010**, *132*, 6124.

(6) Kavan, L.; Zukalova, M.; Kalbac, M.; Graetzel, M. *J. Electrochem. Soc.* **2004**, *151*, A1301.

(7) Wang, Y. J.; Caruso, F. *Adv. Funct. Mater.* **2004**, *14*, 1012.

(8) Burazerovic, S.; Gradinaru, J.; Pierron, J.; Ward, T. R. *Angew. Chem., Int. Ed.* **2007**, *46*, 5510.

(9) Jin, L.; Zhai, J.; Heng, L.; Wei, T.; Wen, L.; Jiang, L.; Zhao, X.; Zhang, X. *J. Photochem. Photobiol., C* **2009**, *10*, 149.

(10) Kim, J.; Bhattacharjee, S.; Jeong, K. E.; Jeong, S. Y.; Choi, M.; Ryoo, R.; Ahn, W. S. *New J. Chem.* **2010**, *34*, 2971.

(11) Kuang, D. B.; Brezesinski, T.; Smarsly, B. *J. Am. Chem. Soc.* **2004**, *126*, 10534.

(12) Fan, W.; Snyder, M. A.; Kumar, S.; Lee, P. S.; Yoo, W. C.; McCormick, A. V.; Penn, R. L.; Stein, A.; Tsapatsis, M. *Nat. Mater.* **2008**, *7*, 984.

(13) Snaith, H. J.; Schmidt-Mende, L. *Adv. Mater.* **2007**, *19*, 3187.

(14) Graetzel, M. *J. Photochem. Photobiol., C* **2003**, *4*, 145.

(15) Graetzel, M. *Nat. Mater.* **2001**, *414*, 338.

(16) Chiba, Y.; Islam, A.; Watanabe, Y.; Komiya, R.; Koide, N.; Han, L. *Jpn. J. Appl. Phys., Part 2* **2006**, *45*, L638.

(17) Guldin, S.; Huttner, S.; Kolle, M.; Welland, M. E.; Muller-Buschbaum, P.; Friend, R. H.; Steiner, U.; Tetreault, N. *Nano Lett.* **2010**, *10*, 2303.

(18) Nishimura, S.; Abrams, N.; Lewis, B. A.; Halaoui, L. I.; Mallouk, T. E.; Benkstein, K. D.; van de Lagemaat, J.; Frank, A. J. *J. Am. Chem. Soc.* **2003**, *125*, 6306.

(19) Mihi, A.; Miguez, H. *J. Phys. Chem. B* **2005**, *109*, 15968.

(20) Halaoui, L. I.; Abrams, N. M.; Mallouk, T. E. *J. Phys. Chem. B* **2005**, *109*, 6334.

(21) Mihi, A.; Calvo, M. E.; Anta, J. A.; Miguez, H. *J. Phys. Chem. C* **2008**, *112*, 13.

(22) Liu, Z.; Subramania, V.; Misra, M. *J. Phys. Chem. C* **2009**, *113*, 14028.

(23) Kuang, D.; Brillet, J.; Chen, P.; Takata, M.; Uchida, S.; Miura, H.; Sumioka, K.; Zakeeruddin, S. M.; Graetzel, M. *ACS Nano* **2008**, *2*, 1113.

(24) Zhu, K.; Vinzant, T. B.; Neale, N. R.; Frank, A. J. *Nano Lett.* **2007**, *7*, 3739.

(25) Kwak, E. S.; Lee, W.; Park, N. G.; Kim, J.; Lee, H. *Adv. Funct. Mater.* **2009**, *19*, 1093.

(26) Pan, H.; Feng, Y. P. *ACS Nano* **2008**, *2*, 2410.

(27) Tetreault, N.; Horvath, E.; Moehl, T.; Brillet, J.; Smajda, R.; Bungener, S.; Cai, N.; Wang, P.; Zakeeruddin, S. M.; Forro, L.; Magrez, A.; Graetzel, M. *ACS Nano* **2010**, *4*, 7644.

(28) Jennings, J. R.; Ghicov, A.; Peter, L. M.; Schmuki, P.; Walker, A. B. *J. Am. Chem. Soc.* **2008**, *130*, 13364.

(29) Zukalova, M.; Zukal, A.; Kavan, L.; Nazeeruddin, M. K.; Liska, P.; Graetzel, M. *Nano Lett.* **2005**, *5*, 1789.

(30) Szeifert, J. M.; Fattakhova-Rohlfing, D.; Georgiadou, D.; Kalousek, V.; Rathousky, J.; Kuang, D.; Wenger, S.; Zakeeruddin, S. M.; Graetzel, M.; Bein, T. *Chem. Mater.* **2009**, *21*, 1260.

(31) Szeifert, J. M.; Feckl, J. M.; Fattakhova-Rohlfing, D.; Liu, Y. J.; Kalousek, V.; Rathousky, J.; Bein, T. *J. Am. Chem. Soc.* **2010**, *132*, 12605.

(32) Prochazka, J.; Kavan, L.; Shklover, V.; Zukalova, M.; Frank, O.; Kalbac, M.; Zukal, A.; Pelouchova, H.; Janda, P.; Mocek, K.; Klementova, M.; Carbone, D. *Chem. Mater.* **2008**, *20*, 2985.

(33) Zukalova, M.; Prochazka, J.; Zukal, A.; Yum, J. H.; Kavan, L. *Inorg. Chim. Acta* **2008**, *361*, 656.

(34) Chou, T. P.; Zhang, Q.; Russo, B.; Fryxell, G. E.; Cao, G. *J. Phys. Chem. C* **2007**, *111*, 6296.

(35) Kim, D.; Ghicov, A.; Albu, S. P.; Schmuki, P. *J. Am. Chem. Soc.* **2008**, *130*, 16454.

(36) Albu, S. R.; Kim, D.; Schmuki, P. *Angew. Chem., Int. Ed.* **2008**, *47*, 1916.

(37) Costacurta, S.; Biasetto, L.; Pippel, E.; Woltersdorf, J.; Colombo, P. *J. Am. Ceram. Soc.* **2007**, *90*, 2172.

(38) Angelome, P. C.; Fuertes, M. C.; Soler-Illia, G. *Adv. Mater.* **2006**, *18*, 2397.

(39) Wang, T.; Sel, O.; Djerdj, I.; Smarsly, B. *Colloid Polym. Sci.* **2006**, *285*, 1.

(40) Galusha, J. W.; Tsung, C.-K.; Stucky, G. D.; Bartl, M. H. *Chem. Mater.* **2008**, *20*, 4925.

(41) Prochazka, J.; Kavan, L.; Zukalova, M.; Frank, O.; Kalbac, M.; Zukal, A.; Klementova, M.; Carbone, D.; Graetzel, M. *Chem. Mater.* **2009**, *21*, 1457.

(42) Wang, K. X.; Wei, M. D.; Morris, M. A.; Zhou, H. S.; Holmes, J. D. *Adv. Mater.* **2007**, *19*, 3016.

(43) Keilbach, A.; Doblinger, M.; Kohn, R.; Amenitsch, H.; Bein, T. *Chem.-Eur. J.* **2009**, *15*, 6645.

(44) Platschek, B.; Petkov, N.; Himsl, D.; Zimdars, S.; Li, Z.; Kohn, R.; Bein, T. *J. Am. Chem. Soc.* **2008**, *130*, 17362.

(45) Platschek, B.; Petkov, N.; Bein, T. *Angew. Chem., Int. Ed.* **2006**, *45*, 1134.

(46) Alberius, P. C. A.; Frindell, K. L.; Hayward, R. C.; Kramer, E. J.; Stucky, G. D.; Chmelka, B. F. *Chem. Mater.* **2002**, *14*, 3284.

(47) Ito, S.; Murakami, T. N.; Comte, P.; Liska, P.; Graetzel, C.; Nazeeruddin, M. K.; Graetzel, M. *Thin Solid Films* **2008**, *516*, 4613.